Impedance of RF shield on ceramic chamber in the rapid cycling synchrotron of China Spallation Neutron Source*

Liang-Sheng Huang,[1,2,3,†] Bin Wu,[1,2] Ming-Yang Huang,[1,2,3] Ren-Hong Liu,[1,2] Biao Tan,[1,2] Peng-Cheng Wang,[1,2] Yong-Chuan Xiao,[1,2] Li-Rui Zeng,[1,2,3] and Xiao Li[1,2,3,‡]

[1] *Spallation Neutron Source Science Center, Dongguan, 523803, China*
[2] *Institute of High Energy Physics, CAS, Beijing, 100049, China*
[3] *University of Chinese Academy of Sciences, Beijing 100049, China*

In a rapid cycling synchrotron (RCS), the magnetic field is synchronized with the beam energy, creating a highly dynamic magnetic environment. A ceramic chamber with a shielding layer (RF shield), composed of a series of copper strips connected a capacitor at either end, is typically employed as the vacuum chamber to mitigate eddy current effects and beam coupling impedance. Consequently, the ceramic chamber exhibits a thin-walled, multilayered complex structure. Previous theoretical studies suggest that the impedance of such a structure has a negligible impact on the beam. However, recent impedance measurements of the ceramic chamber in the China Spallation Neutron Source (CSNS) RCS reveal a resonance in low-frequency range, which further theoretical analysis confirms as a source of beam instability in the RCS. Currently, the magnitude of this impedance cannot be accurately assessed through theoretical calculations. In this study, we utilize CST Microwave Studio to confirm the impedance of the ceramic chamber. Further simulations covering six different types of ceramic chambers are conducted to develop an impedance model in the RCS. Additionally, this paper investigates the resonant characteristics of the ceramic chamber impedance, finding that the resonant frequency is closely related to the capacitance of capacitors. This finding provides clear directions for further impedance optimization and is crucial for achieving the beam power of 500 kW for the CSNS Phase II project (CSNS-II). However, careful attention must be given to the voltage across the capacitors.

Keywords: Beam coupling impedance, ceramic chamber, RF shield, resonance, high dynamic magnetic environment

I. INTRODUCTION

The China Spallation Neutron Source (CSNS) is a high-intensity proton accelerator-based facility [1, 2], which is designed to provide multidisciplinary platforms for scientific research and applications [3–6]. The accelerator complex consists of two primary components: a Negative Hydrogen (H^-) Linac [7–10] and a Rapid Cycling Synchrotron (RCS) [11]. The H^- beam from the Linac is injected into the RCS through a multi-turn charge-exchange process [12]. Within the RCS, two proton bunches, with a total of $N_p = 1.56 \times 10^{13}$ per pulse, are accelerated from 80 MeV to 1.6 GeV at a repetition rate of 25 Hz. Currently, the RCS provides a beam power of 100 kW on the target. In the Phase-II of CSNS (CSNS-II), the beam power on the target will be upgraded from 100 kW to 500 kW by increasing the beam intensity. The RCS is dominated by space charge effects. To address these, superconducting cavities will be utilized to boost the Linac beam energy from 80 MeV to 300 MeV, mitigating the space charge effects in the RCS. Following these upgrades, the accumulated number of protons in the RCS is expected to reach $N_p = 7.8 \times 10^{13}$ per pulse.

TABLE 1 presents the main parameters of the RCS, which employs a triplet four-fold symmetric lattice structure with a circumference of 227.92 meters. It consists of 24 dipole magnets and 48 quadrupole magnets, energized by a 25 Hz DC-biased sinusoidal current pattern [13, 14]. The RCS has a nominal tune of (4.86 , 4.78) and a natural chromaticity of (-4.2 , -9.1). The DC sextupole field is designed to improve chromaticity control and minimize beam loss at injection. The magnetic field is synchronized with beam energy, resulting in a highly dynamic magnetic environment. Fig. 1 depicts the ramping energy, magnetic field curve, and its rate of change. The acceleration ramp is characterized by a standard sine wave, with a magnetic field change rate exceeding 60 T/s.

TABLE 1. Main parameters of RCS.

Parameters [unit]	Values
Circumference, [m]	227.92
Injection energy of CSNS/CSNS-II, [GeV]	0.08/0.3
Extraction energy, [GeV]	1.6
Repetition rate, [Hz]	25
Ramping pattern	Sinusoidal
dB/dt, [T/s]	63
Number of ceramic chambers	76
Bunch number	2
Bunch intensity of CSNS/CSNS-II, [1×10^{12}]	7.8/39
Nominal tune (H,V)	(4.86,4.78)
Natural chromaticity (H,V)	(-4.2,-9.1)

Due to the heating of eddy current effects [15], traditional metal chambers are inadequate in such dynamic magnetic environment of the RCS; hence, ceramic chambers are employed. The main part of the chamber is ceramic. To mitigate the leakage field induced by the beam due to the non-conductive nature of ceramic chambers, an RF shield is finally used to reduce eddy current effects and beam coupling impedance. These ceramic chambers are utilized in mag-

* Supported by the Guangdong Basic and Applied Basic Research Foundation, China (Project: 2021B1515140007)
† Corresponding author, huangls@ihep.ac.cn
‡ Corresponding author, lixiao@ihep.ac.cn

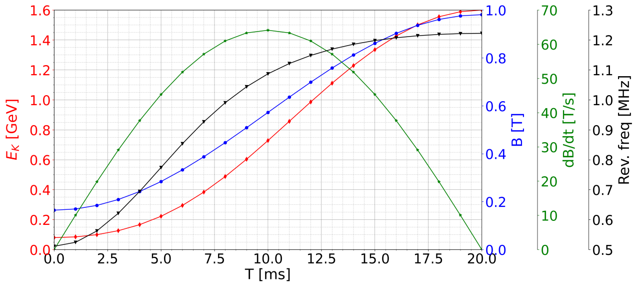

Fig. 1. (Color online) Ramping energy, magnetic curve and change rate of magnetic field in CSNS/RCS.

nets with a high dynamic magnetic field. A ceramic chamber [16] in the CSNS was designed based on existing chamber [17, 18]. The inner surface of the ceramic chamber is coated with a TiN film to reduce secondary electron emission. Surrounding the ceramic, an RF shield is composed of a series of copper strips and capacitors, creating a high-pass filter that mitigates eddy current effects and reduces beam coupling impedance. The ceramic chamber occupies about 130 meters of the RCS, while stainless-steel chambers take the remaining space.

Beam instability associated with ceramic chambers has been observed in RCS facilities worldwide. The head-tail effects [19] were identified in the RCS of ISIS [17] many years ago, and the ceramic chamber has recently been implicated as a potential contributor to impedance [20]. In the RCS of the Japan Proton Accelerator Research Complex (J-PARC) [18], an instability [21] was detected during beam commissioning, appearing before 2 ms when the horizontal and vertical tunes were set to $\nu_x = \nu_y = 5.86$. This beam behavior is analogous to that observed in the RCS of CSNS.

In 2019, the RCS of CSNS experienced an unforeseen instability in the transverse plane as beam power was gradually increased from 20 kW to 50 kW, with the instability worsening at higher power levels [22]. Measurements identified this issue as a transverse coupled bunch instability (TCBI). To address this, tune tracking pattern adjustments and chromaticity optimization using DC-powered sextupole magnets were applied, successfully achieving the designed beam power of CSNS [22, 23]. In 2021, DC sextupole magnets were replaced with AC versions and their associated power supplies [24], providing dynamic chromaticity control over the acceleration cycle. Furthermore, a pulsed octupole magnet was proposed and developed in summer 2023 to mitigate instability under increased beam power. With the aid of AC sextupole and pulsed octupole magnets, the RCS beam power has been increased to 160 kW. Despite these improvements, the beam power has reached the limits of current mitigation strategies, presenting a considerable challenge to the 500 kW objective of CSNS-II. Additionally, the inability to accurately identify the sources of impedance remains a critical issue. If the components contributing to impedance are precisely identified, reducing their impedance could provide a fundamental strategy for increasing beam power, surpassing the effectiveness of existing suppression methods.

The driving forces behind beam instabilities in accelerators depend on the interaction between charged particles and their environment, typically described by beam coupling impedance [25–27]. The RCS of CSNS incorporates components that are widely used and have been effective in other accelerator systems. Despite this, we conducted an extensive impedance analysis for each component of the RCS [28]. Notably, instabilities originating from the stainless-steel chamber [29] and extraction kicker [30] were anticipated to be negligible. Furthermore, the real part of impedance from ceramic chambers [31, 32] was expected to be minimal. It should be noted that the ceramic chamber was modeled as an infinitely long, multi-layered structure with perfect RF shielding, which significantly differs from the actual RF shielding setup.

Recent bench measurements have confirmed that the RF shield on the ceramic chamber is a source of impedance [33]. This represents a novel source of impedance, with relatively limited international research to date. The earliest work on infinitely long ceramic chambers was conducted by Zotter [34] in 1970. Since then, the model has primarily evolved, particularly in the field matching method for both relativistic and non-relativistic particles [35–38]. Danilov has developed an impedance model to estimate the impedance for a finitely long chamber [39]. In these models, electromagnetic fields are assumed to be fully shielded by metal strips, resulting in very low calculated impedance with no predicted resonances. Given the limitations of theoretical calculations, this study employs CST Microwave Studio [40] to simulate the impedance of the ceramic chamber. The simulation validates the existence of resonant impedance and allows for the determination of impedance characteristics for all ceramic chambers in the RCS.

The paper is organized as follows: Sec. II provides a brief overview of RCS instability characteristics. Sec. III reports preliminary impedance measurements of a ceramic chamber. Sec. IV discusses the simulation techniques used to evaluate ceramic chamber impedance and calculates the total impedance for the RCS. The simulations indicate an unexpectedly high impedance in the RCS, presenting a substantial challenge for the CSNS-II project. As a result, Sec. V explores chamber parameters to identify effective impedance reduction methods. The findings suggest that optimizing capacitor capacitance is an effective technique, with capacitor voltage being a key factor. Consequently, Sec. VI provides a detailed theoretical analysis of capacitor voltage, serving as a reference for subsequent impedance reduction practices. The study is summarized and discussed in Sec. VII.

II. CHARACTERISTIC OF THE RCS INSTABILITY IN CSNS

The instability in the RCS was observed at a beam power of approximately 50 kW. Beam measurements have confirmed that it is a TCBI. Under normal tune and natural chromaticity, the beam position in the horizontal plane began to oscillate at around 8 ms. This instability was found to be dependent on beam population, regardless of whether particles were filled

into single or double buckets. The coupled bunch mode was identified as mode one, which means that the betatron oscillation of two bunches is out of phase. The instability exhibited sensitivity to chromaticity, prompting the introduction of sextupole magnets to mitigate this issue. The horizontal tune also had a significant impact on this instability. Fig. 2 illustrates the measured Turn-by-Turn (TbT) beam positions and transmission efficiency in the RCS at different tunes with a beam power of 100 kW. The instability is observed when the tune is below 5.0 , and its occurrence time shifts later as the tune increases. Furthermore, with tested tune during the beam commissioning, the instability in vertical plane can also be observed as beam power increases. If there are M identical equally spaced bunches, the growth rate of the coupled bunch instability $1/\tau_m$ can be theoretically expressed as [41]

$$\frac{1}{\tau_m} = -\frac{eMI_b\omega_0}{4\pi\beta E_0}\frac{\sum_q Re[\beta_\perp Z_T(\omega_q)]h_m}{B\sum_q h_m}F_m. \tag{1}$$

where, e is the electronic charge, I_b is the bunch current and ω_0 is the revolution angular frequency. E_0 is the beam energy with the relativistic velocity factor β. $\beta_\perp$ is average betatron function. B is the bunching factor, defined as the ratio of bunch length to bunch spacing. With coupled mode μ, $Z_T(\omega_q)$ is the impedance magnitude at frequency $\omega_q = ((qM + \mu) + \nu_x + m\nu_s)\omega_0$ with synchrous tune ν_s. For the head-tail mode m, h_m is the power spectrum with the form factor F_m, as specified in Ref. [41]. Within the RCS, q=-3, M=2, μ=1 and m=1, TABLE 2 roughly summarizes the instability occurrence time, energy, β, revolution frequency f_0, tune, and $\omega_q/2\pi \approx 0.13$ MHz.

Our comprehensive studies have provided valuable insights and practical guidance for mitigating instability, particularly through the optimization of tune and chromaticity [23, 33]. To achieve better control over the tune spread and further suppress the instability, the DC sextupole field has been upgraded to an AC sextupole field [24], aiming to provide dynamic for controlling the chromaticity and enhance the beam transmission efficiency over an acceleration cycle.

TABLE 2. Overview of key parameters for RCS instability, roughly closed to the biggest oscillation amplitude of beam position, where $f_r = \omega_q/2\pi$ at q=-3, M=2, μ=1, and m=1.

Parameter [unit]	ν_x=4.78	ν_x=4.83	ν_x=4.86	ν_x=4.89
Occurrence time [ms]	~ 2	5	7.0	~ 14
E_0 [GeV]	0.11	0.22	0.42	1.3
β	0.441	0.585	0.722	0.905
f_0 [MHz]	0.58	0.77	0.95	1.19
ν_s	0.01	0.0085	0.005	0.002
f_r [MHz]	0.127	0.131	0.132	0.13

III. BENCH MEASUREMENT OF A CERAMIC CHAMBER

To mitigate eddy current effects and ohmic losses, ceramic chambers are employed in the AC magnets, including the dipole, quadrupole, and injection painting magnets in the RCS of CSNS. As detailed in reference [16] and depicted in Fig. 3, these chambers feature a three-layer tube design. The inner surface is coated with a 100 nm layer of Titanium Nitride (TiN) to reduce secondary electron emission. Given the non-conductive nature of ceramics, an RF shield composed of 0.4 mm thick Cu plates, waterjet-cut into 5 mm wide strips with 5 mm spacing, is utilized to decrease the impedance of the image current. Each Cu strip is segmented to prevent current loops, effectively suppressing eddy current effects. Furthermore, connecting the strip segments with capacitors (with a capacitance of 330 nF) creates an RF shield with a high-frequency pass filter, which reduces both eddy current effects and beam coupling impedance. TABLE 3 summarizes the shape, length, and thickness of the chambers. An elliptical chamber is used for the dipole magnet, while circular cross-section chambers are employed for the others. The RCS comprises six types of ceramic chambers, with a total length of approximately 130 meters, distributed across 76 units.

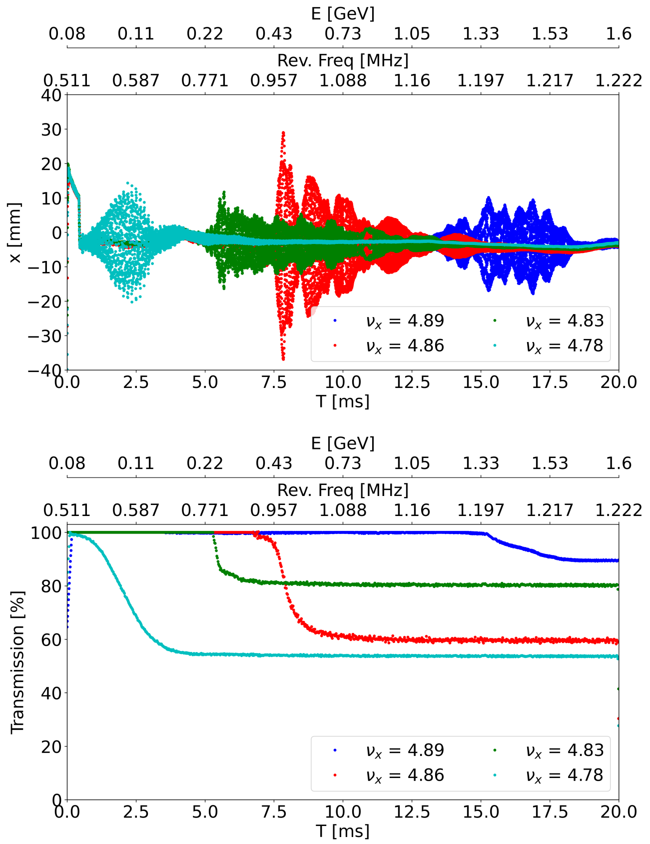

Fig. 2. (Color online) The TbT beam position (top) and RCS transmission efficiency (bottom) at different horizontal tunes with natural chromaticity at a beam power of 100 kW. The vertical tune is kept at 4.75.

To identify the impedance, a ceramic chamber located in the injection area (INB1) is utilized to measure impedance. The conventional wire method is employed for coupling impedance measurements. For transverse impedance measurements, the standard technique involves the twin-wire

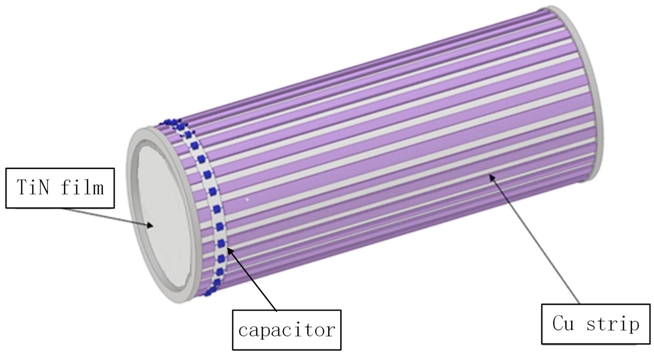

Fig. 3. (Color online) Illustration of the ceramic chamber.

TABLE 3. Parameters of the RCS Ceramic Chamber.

Name	Shape	Length [m]	Size [mm]	Thickness [mm]	Number
MB[a]	elliptic	2.775	218×135	15×8.5	24
QA	circular	0.78	91.5	7.5	16
QB	circular	1.535	124.5	7.5	16
QC	circular	1.54	99.5	7.5	8
QD	circular	1.205	115	7.5	8
INB[b]	circular	1.1	80	7.5	4

[a] The size and thickness mean horizontal × vertical size for MB with an elliptic cross-section.
[b] There are two similar types of injection chambers, and simplifies as one here.

method, where two parallel wires carrying out-of-phase signals are inserted through the Device Under Test (DUT) to generate a dipole current moment, and the forward scatter coefficient, S_{21}, is measured covering the frequency range $< 100\,\mathrm{MHz}$. We have not observed unexpected impedance in such frequency range. However, due to significant measurement errors associated with the twin-wire method at low frequencies, the loop method is more suitable for this measurement, as illustrated on the top of Fig. 4. The equipment for loop measurements includes a Vector Network Analyzer (VNA), a hybrid, and the DUT. The out-of-phase signal is generated by the hybrid. The loop probe comprises two parallel wires with shorted ends. The spacing Δ of the Cu wires is $40\,\mathrm{mm}$, with a wire diameter of $0.5\,\mathrm{mm}$. The reflection coefficient, S_{11}, is measured and the input impedance for DUT, Z_{in}^{DUT}, is given [42]

$$Z_{in}^{DUT} = \frac{2Z_0 S_{11}}{1 - S_{11}}, \tag{2}$$

with characteristic impedance Z_0. The transverse impedance can be expressed [43] as

$$Z_T = \frac{c}{\omega} \frac{Z_{in}^{DUT} - Z_{in}^{REF}}{\Delta^2}, \tag{3}$$

with measured frequency ω and the speed of light c. The measured input impedance, Z_{in}^{REF}, corresponds to a smooth, homogeneous beam chamber of equal length (REF), using the ceramic chamber without the RF shield as REF in the measurement.

The impedance $< 10\,\mathrm{MHz}$ is measured and a sharp resonance peak is detected. The real part of the impedance is presented in the bottom of Fig. 4. The center frequency is $0.123\,\mathrm{MHz}$, aligning perfectly with the beam measurement results, $\sim 0.13\,\mathrm{MHz}$. To investigate the source further, the RF shield was removed during measurement, leading to the disappearance of the resonance. Notably, the INB1 chamber measured was not coated by the TiN film. Impedance measurements were repeated after TiN coating, and the impedance persisted. Consequently, it was determined that the resonance originates from the RF shield.

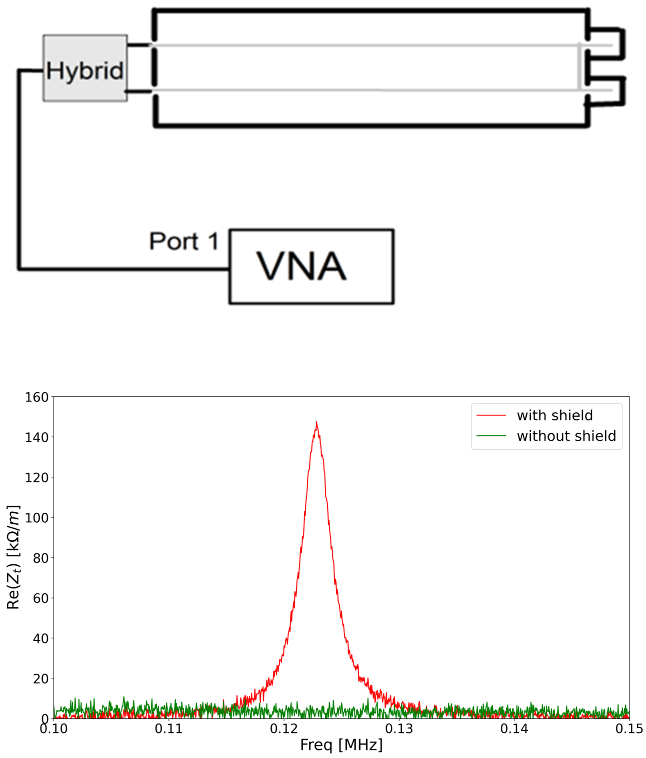

Fig. 4. (Color online) Schematic setup of the transverse impedance measurement with one loop method (top) and measured real part of INB1 transverse impedance (bottom).

IV. NUMERICAL SIMULATION

To verify the impedance of the ceramic chamber, numerical simulations are conducted using the CST simulation suite. Actually, the wake field of ceramic chamber were simulated using Particle STUDIO many years ago, but no resonance was detected. In contrast, simulation with Microwave STUDIO recently revealed the resonance. This discrepancy may be from meshgrids: Particle STUDIO employs only hexahedral meshgrid in the time domain, while Microwave STUDIO utilizes tetrahedral meshgrid in the frequency domain (the hexahedral meshgrid is unable for capacitors in frequency domain). To further investigate this phenomenon, a time-domain model with hexahedral meshgrids was constructed

in Microwave STUDIO and recomputed, but resonance remained undetected. This hypothesis will be further investigated as the software undergoes upgrades.

In the simulation, several reasonable simplifications are applied to develop a physical model that closely resembles the actual chamber. A simplified representation of the chamber is depicted in Fig. 5. The primary components of the chamber include ceramic and two titanium ports at each end, consistent with the real chamber. The thin TiN film inside is omitted. The RF shield covering the ceramic consists of Cu strips and capacitors, consistent with the real design. We assume the capacitor has a loss of $0.09\ \Omega$. The Kapton film, used in the real chamber for its high radiation resistance, is ignored due to its non-conductive nature. The chamber length is 1.07 meters. A loop probe, similar to that in the measurement, is incorporated in the simulation using two parallel wires with shorted ends, matching the 0.5 mm diameter of the measurement wires. A discrete port is provided to calculate the reflection scattering coefficient at the open port. The size of meshgrid is automatically adjusted based on regional dimensions, thereby improving calculation accuracy and optimizing memory and time usage. Approximately one million meshgrids are utilized to ensure precise results. A REF simulation is done on a stainless-steel chamber with equal length.

The input reflection coefficients for both the DUT and REF are simulated, and the corresponding input impedances are provided in Eq. (2). The simulated impedance of the ceramic chamber is shown in Eq. (3) and illustrated in Fig. 6. To enhance clarity, the measured results from Fig. 4 are also displayed. The resonant frequency identified closely corresponds to the measured results, thereby confirming the impedance in the simulation.

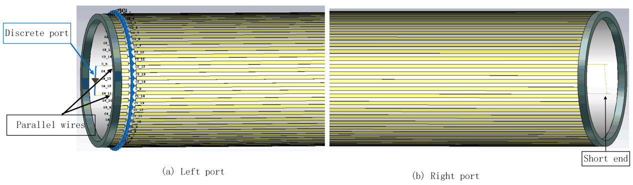

Fig. 5. (Color online) Simulated model of the ceramic chamber.

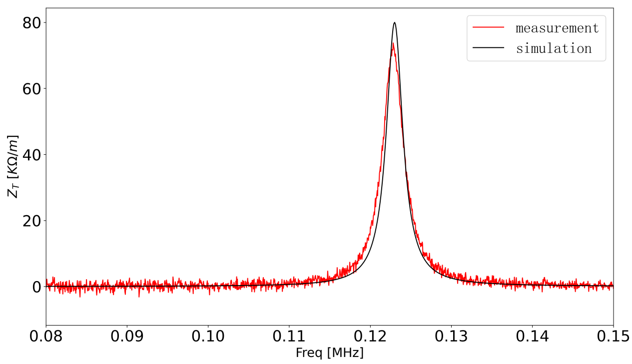

Fig. 6. (Color online) Simulated transverse impedance of the INB1 and compared with that of measurement.

After accurately confirming the INB1 impedance, we simulated the impedances of all chamber types in the RCS and developed a comprehensive impedance model including all ceramic chambers, as illustrated in Fig. 7. Each ceramic chamber exhibits resonance in the low-frequency range, with resonant frequencies varying among the different chambers. TABLE 4 provides a detailed summary of the resonant parameters for all chambers in the RCS. The resonant frequencies range from 70 kHz to 150 kHz, with Q-values below 150. The MB chamber in the dipole magnet exhibits the highest impedance, reaching $6\ \mathrm{M\Omega/m}$.

In our simulations, we employed a monitor to evaluate the electromagnetic field at the resonant frequency. The findings indicate that the induced electromagnetic field predominantly propagates along the Cu strips, with some leakage beyond the vacuum chamber. Such leakage may cause disturbances due to external magnet yokes, thereby influencing the resonance. The ceramic chambers in the RCS are predominantly encircled by dipole and quadrupole magnets. To explore this phenomenon, simplified models of the magnet yokes were developed, modeled as perfect electric conductors (PEC) with a thickness of 20 mm. The resonant frequencies of the chamber with and without the yokes are compared in TABLE 4. The results demonstrate that the presence of the yokes induces a shift in resonance frequency, which varies among different chamber configurations. For chambers with circular cross-sections, the yoke-induced frequency shift is negligible. However, for the MB chamber with an elliptical cross-section, where the yoke is 2.1 m long and closely aligned with the chamber in the vertical plane, the resonant frequency increases significantly, reaching approximately 35 kHz, indicating a substantial effect.

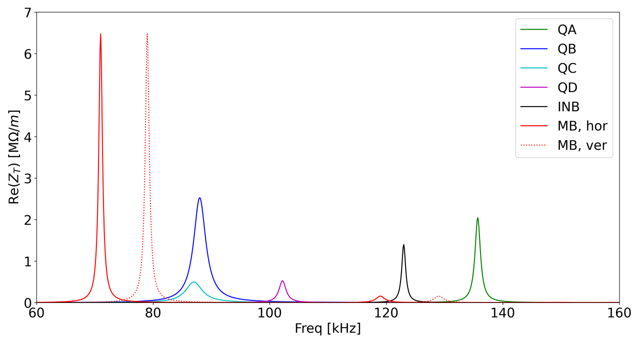

Fig. 7. (Color online) Impedance of all ceramic chambers in the RCS. Because of the circular cross-section for MB chamber, the horizontal impedance differs from the vertical impedance.

V. INVESTIGATION OF IMPEDANCE REDUCTION TECHNIQUES

The unusually high impedance illustrated in Fig. 7 explains the instability encountered during the RCS beam commissioning at low power levels. Achieving the design power target of 500 kW for CSNS-II needs the reduction of ceramic

TABLE 4. Comparison of resonance frequency between ceramic chamber with and without yoke.

Name	f_r without yoke [MHz]	f_r with yoke [MHz]
MB, Z_h	0.071	0.085
MB, Z_v	0.079	0.114
QA	0.136	0.141
QB	0.088	0.098
QC	0.087	0.1
QD	0.102	0.109
INB	0.123	0.127

chamber impedance in the RCS. Accordingly, we undertook a series of simulation studies to explore effective impedance reduction strategies. In this context, the feasibility and cost-effectiveness of these techniques are critical considerations. Therefore, our objective is to identify the most dependable methods for impedance reduction, rather than focusing exclusively on the optimal solution.

Using the INB1 as a reference, we performed detailed scans of various parameters, such as the strip number, width, and thickness, along with the chamber radius and length, and the capacitor capacitance. The simulations demonstrate that the resonant frequency is mostly unaffected by the strip number, width, and thickness, as well as the chamber radius. Rather, it is determined by the length of ceramic chamber and the capacitance of capacitors.

The impedance for various chamber lengths is examined, showing a decrease in resonant frequency with increasing vacuum chamber length. However, since the chamber length is fixed in practical accelerators, this aspect will not be further explored in this article. Moreover, the resonant impedance for different capacitor capacitances is also simulated, with results displayed on the top of Fig. 8. It is evident that as capacitance increases, both the resonant frequency and peak impedance decrease. The lower figure provides a summary of resonant frequencies for various capacitances. With a given capacitance of the capacitor C, the resonant frequency is calculated in theoretically by

$$f_r = \frac{1}{\sqrt{2\pi L_0 C}}, \tag{4}$$

with a constant inductance L_0 = 1.0146 $\times$ 10^{-5} H. The calculated resonances show excellent agreement with the simulation results, suggesting that the impedance issue can be simplified to addressing the inductance of the RF shield.

In a word, the simulations demonstrate that adjusting the capacitance of capacitors can effectively reduce impedance. Nonetheless, careful experimental validation is essential before applying this strategy to the RCS to ensure its reliability, with particular attention to the voltage across the capacitors.

VI. INDUCED VOLTAGES ON CAPACITORS

During the ramping process in the RCS, voltages are induced on the capacitors. If these voltages exceed the rated threshold, capacitor failure may occur, leading to distortions

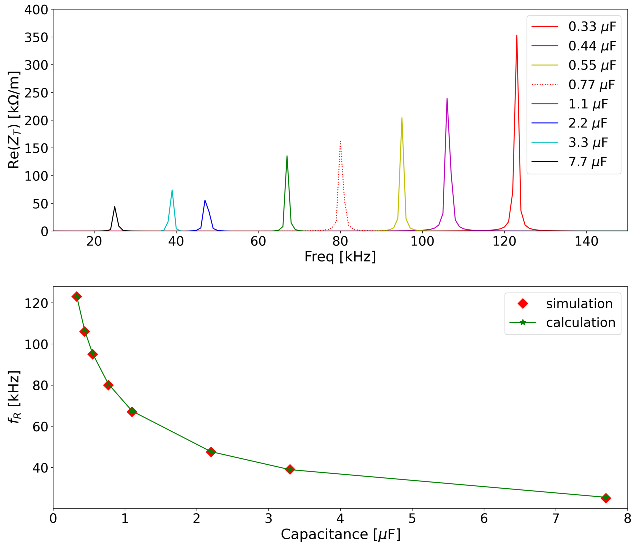

Fig. 8. (Color online) The top figure presents the simulated impedance across different capacitance values. The bottom figure compares the simulated resonant frequency on them with theoretical calculations by $f_r = 1/\sqrt{2\pi L_0 C}$, with a fitted inductance L_0 = 1.0146 $\times$ 10^{-5} H.

in the magnetic field and subsequent beam instability. This instability has been empirically observed in the RCS of J-PARC as a result of these field distortions [44]. The voltage on capacitors is generated by both the beam and the dynamic magnetic field. In accelerators, circular vacuum chambers are the predominant structural configuration. Therefore, this study will focus on examining the voltage within circular cross-sections.

A. Voltages on capacitors from dynamic magnetic field

The induced electromotive force, V, is proportional to the rate of change of magnetic flux linking the circuit, as dictated by Faraday's law of electromagnetic induction

$$V = -\frac{d(B \cdot S)}{dt}, \tag{5}$$

with the time rate of change of magnetic field dB/dt and the cross-sectional area of a strip circuit S. The inner radius of the cylindrical RF shield is given by r. For simplicity, we focus on the central plane, which maximizes the cross-sectional area, as depicted in Fig. 9(a). We assume that the longitudinal magnetic field components can be neglected, which allows us to simplify Fig. 9(a) to the form shown in Fig. 9(b). Furthermore, we consider only the case where the strip is cylindrical with a radius b, the cross-sectional area S can be expressed as $S = 2(r + b)L$ with a magnet length L. Generally, since $r \gg b$ the area can be approximated as $S = 2rL$.

In the RCS of CSNS-II, a transverse painting technique is utilized during injection to ensure beam uniformity and reduce space charge effects. New rectangular chamber (BCH)

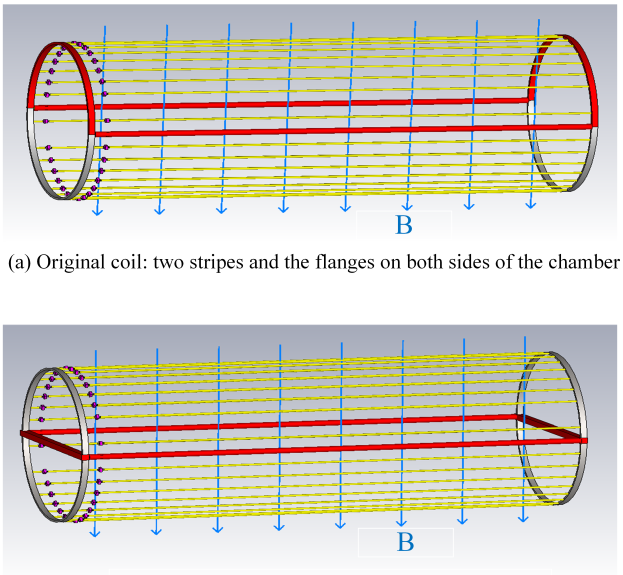

(a) Original coil: two stripes and the flanges on both sides of the chamber

(b) Simplified coil: two stripes and simplified ends

Fig. 9. (Color online) The schematic picture of coil with the biggest area on the RF shield of ceramic chamber. (a) is the original coil and (b) is the simplified one.

with a bigger size of 245 mm × 167 mm and length of 0.44 m will be implemented. The injection system consists of horizontal and vertical painting magnets. The painting magnetic field exhibits the highest temporal rate of change. As illustrated in Fig. 10, the typical magnetic field profile for these magnets includes a rise time (from 0 to t_1), a flat-top time (from t_1 to t_2), a painting time (from t_2 to t_3), and a fall time (from t_3 to 1.2 ms). During the fall phase, the rate of change of the magnetic field reaches a peak of dB/dt =3660 T/s, inducing a voltage of approximately 320 V, thereby justifying the use of capacitors. Additional evaluations were conducted to determine the voltage that capacitors on all vacuum chambers must withstand, taking into account the dimensions of the RCS vacuum chamber and the change rate of magnetic field, as detailed in TABLE 5. It is clear that, apart from the injection region, the voltage endured by other capacitors is significantly lower.

TABLE 5. The voltage on the capacitor of ceramic chamber.

Chamber in magnet	dB/dt [T/s]	Volt [V]
Dipole magnet	60	27.5
Quadrupole magnet	61	15
Painting magnet	3660	314

B. Voltages on capacitors from beam

When the beam travels along the ceramic chamber, the beam current is easily given as

$$I = \hat{\lambda} e \beta c, \tag{6}$$

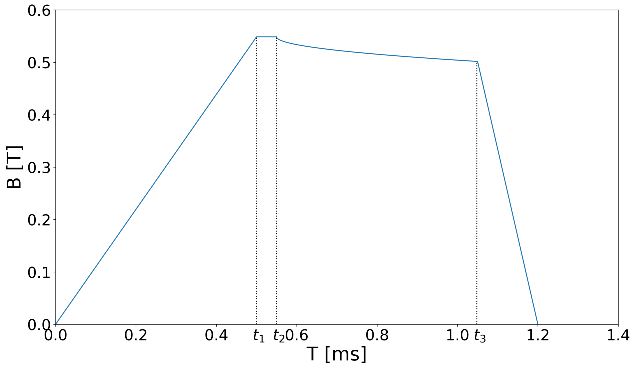

Fig. 10. (Color online) The typical magnetic field profile of the painting magnets in the RCS of CSNS.

where e is the electric charge and β is the relativistic velocity factor. For Gaussian beam with bunch length σ_z, the peak line charge density $\hat{\lambda}$ can be expressed [25] as

$$\hat{\lambda} = \frac{N_b}{\sqrt{2\pi}\sigma_z}, \tag{7}$$

with particle number in the bunch N_b. The Gauss's law gives the electric field at strips with distance r as

$$E = \frac{\hat{\lambda} e}{2\pi\varepsilon_0 r}, \tag{8}$$

with dielectric constant ε_0. Due to the beam line charge inducing image charges on the strips, the electric field outside the vacuum chamber remains zero. Therefore, the line density of image charges is

$$\sigma_s = \varepsilon_0 E = \frac{\hat{\lambda} e}{2\pi r}. \tag{9}$$

For a monopole beam located at the center of the chamber, the total induced image charge on the chamber is accurately equal to the charge of the source beam as $2\pi r \cdot \sigma_s = \hat{\lambda} e$, ensuring self-consistency. In practice, the shield of the chamber is composed of many strips. It is assumed that the leakage of the magnetic field beyond the chamber is negligible. Therefore, the Eq. (9) can be simplified to

$$\sigma_s = \frac{\hat{\lambda} e}{dN_s}. \tag{10}$$

with strip number dN_s. The current on a strip is $I_s = I/dN_s$. For the dipole beam with a shift x in horizontal plane in Fig. 11, we typically have $x \ll r$ and the voltage varies across different strips. A cylindrical coordinate system (r,θ) is adopted to describe the chamber with circular cross-section, with θ as the azimuthal coordinate. The strip positions are given by ($r\cos\theta$,$r\sin\theta$). The distance from the strips to the beam is described as

$$d = \sqrt{x^2 - 2rx\cos\theta + r^2}, \tag{11}$$

and the line density of image charges becomes

$$\sigma'_s = \frac{\hat{\lambda} e}{2\pi d}. \tag{12}$$

The current on strips is easily given and simplified as

$$I' = I\frac{r}{d}, \tag{13}$$

and the current on a strip is $I'_s = I'/dN_s$.

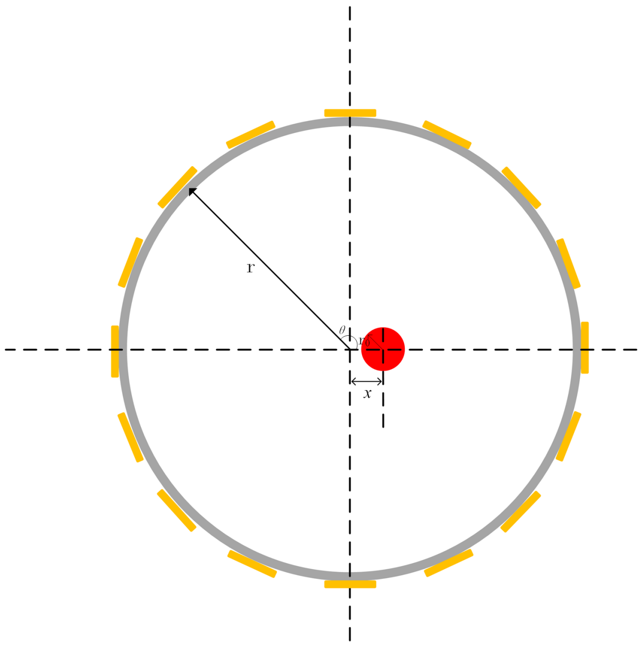

Fig. 11. (Color online) The schematic picture of the RF-shielded chamber. The grey is ceramic and the red is beam with a shift x. The yellows are Cu strips. Each of the strips is defined by $(r\cos\theta, r\sin\theta)$), with $\theta = 2\pi i/dN_s$ and $i = 0, 1, 2, \cdots, dN_s - 1$. The conditions meet $x \ll r$ and $r_0 \ll r$.

The resistance of the strip is given by

$$R_s = \rho\frac{L_s}{A}. \tag{14}$$

where, ρ is resistivity, L_s is the length of Cu strips, and A is a cross-sectional area. For the skin depth δ_s and width of rectangular strip w, $A = \delta_s w$.

With the resistance of strips, the voltage across the capacitor is determined by the current flowing through the strip as

$$V = I'_s R_s. \tag{15}$$

The typical parameters of the beam and the ceramic chamber in the RCS are presented in TABLE 6. For a typical ceramic chamber with $dN_s = 66$, the beam intensity peaks at 77 A during extraction, serving as a representative case for voltage estimation. The skin depth $\delta_s = 30$ μm at a typical beam frequency of 5 MHz. Each Cu strip, with a length of 2.1 m, has a resistance of approximately 0.24 Ω. Fig. 12 illustrates the voltage on capacitors at different azimuthal angles and a beam with various shift. It is easy to see that the voltage changes with the horizontal shift and azimuthal angle. For a monopole beam, the voltage on the strip is about 0.28 V. In the case of a dipole beam with a 60 mm shift, the maximum voltage on the capacitors is approximately 0.55 V, which is considered negligible compared to the voltage induced by external magnetic fields.

TABLE 6. Main parameters of beam and chamber in the RCS.

Parameter [unit]	Valus
σ_z at injection/extraction [m]	20/9
β at injection/extraction	0.38/0.93
I_b at injection/extraction [A]	14/77
Length of chamber L [m]	2.1
Radius of chamber r [m]	0.1
Strip number dN_s	66
Strip width w [mm]	5
Strip thickness t [mm]	0.4
Resistivity of strips [$\Omega \cdot$ m]	1.7×10^{-8}

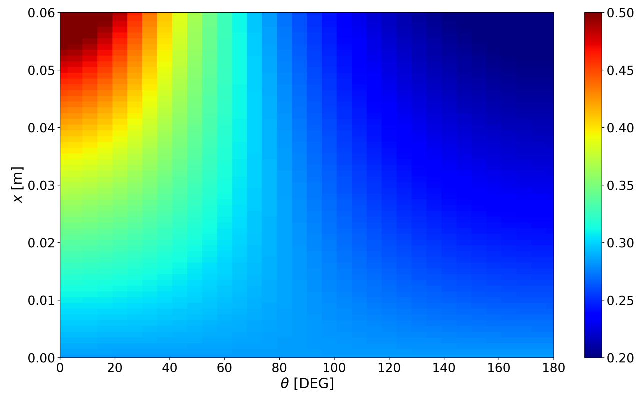

Fig. 12. (Color online) Voltage on capacitors at different azimuthal angles and a beam with a shift x. where a typical ceramic chamber in the RCS with number of Cu strip of 66 and length 2.1 m, and the beam intensity of 77 A with frequency at 5 MHz at extraction is used.

VII. CONCLUSION AND OUTLOOK

An unexpected transverse instability was detected at low beam power during the beam commissioning phase in the RCS of CSNS. Subsequent measurements identified this instability as a TCBI. By optimizing the tune and chromaticity, the instability was effectively suppressed, allowing for the current achievement of 160 kW beam power. Nonetheless, achieving the 500 kW goal for CSNS-II poses a considerable challenge. Consequently, studying the impedance sources is still essential. Beam measurements indicate a possible resonance with a significantly large impedance. Impedance measurements confirmed a resonance associated with the RF shield on the ceramic chamber, aligning with the frequency observed in beam measurements. Simulations conducted using CST Microwave Studio replicate this impedance. As this

new impedance cannot be theoretically calculated, we have developed an impedance model for the RCS ceramic chambers based on the simulation, providing a foundation for further analysis of beam effects.

Preliminary numerical simulations have provided insights into the physical principles behind impedance, thereby contributing to the enhancement of chamber design for impedance reduction. The simulations investigate key parameters such as chamber length, capacitor capacitance, and the effect of the magnet yoke. From a practical and cost-effective perspective, optimizing capacitor capacitance is identified as a promising approach to reducing impedance. Although these simulations offer a comprehensive understanding of the impedance characteristics of ceramic chambers and propose effective reduction strategies, thorough validation is required before practical application, with particular attention to the voltage on capacitors.

This research is currently in its initial phase. While simulation studies have offered valuable insights into the impedance characteristics of the ceramic chamber in the RCS, further research is crucial. This involves exploring additional strategies for impedance reduction and the impact of electromagnetic fields in the accelerator tunnel. Moreover, the detailed simulation results require interpretation through comprehensive impedance and beam physics theory. Consequently, future work will focus on theoretical analysis and the exploration of techniques for reducing impedance.

ACKNOWLEDGEMENTS

The authors would also like to thank Wei-Dong Chen for many discussions and comments in the measurement and simulation. We would like to acknowledge the support of Sheng-Yi Chen, Sheng-Hua Liu and Hai-Bo Li in the measurement. This work is supported by the Guangdong Basic and Applied Basic Research Foundation, China (Project: 2021B1515140007).

[1] J. Wei, H. S. Chen, Y. W. Chen, et al., China Spallation Neutron Source: Design, R&D, and outlook. Nucl. Instrum. Methods Phys. Res. A. **600(1)**, 10–13 (2008). doi: 10.1016/j.nima.2008.11.017

[2] S. Wang, S. X. Fang, S. N. Fu, et al., Introduction to the overall physics design of CSNS accelerators. Chinese Physics C **33(S2)**, 1-3 (2009). doi: 10.1088/1674-1137/33/S2/001

[3] L. Dong, J. Zhang, Y. Li, et al., Borrowed dislocations for ductility in ceramics. Science **385(6707)**, 422-427 (2024). doi: 10.1126/science.adp0559

[4] J. Wang, J. Ren, W. Jiang, et al., In-beam gamma rays of CSNS Back-n characterized by black resonance filter. NUCL SCI TECH **35(10):164** (2024). doi: 10.1007/s41365-024-01553-8

[5] Y. Hong, Y. Song, L. Zhou, et al., Beamline design for multipurpose muon beams at CSNS EMuS. NUCL SCI TECH **35(5):38** (2024). doi: 10.1007/s41365-024-01406-4

[6] S. Xiao, Y. He, Z. He, et al., Driving system design and precision test of the VSANS detector trolleys. Nuclear Techniques **45(9):090401** (2022). doi: 10.11889/j.0253-3219.2022.hjs.45.090401

[7] S. Liu, T. Huang, H. Ouyang, et al., Status of CSNS H^- ion source. Chinese Physics C **39(5):057008** (2015). doi: 10.1088/1674-1137/39/5/057008

[8] Y. Xiao, H. Ouyang, K. Xue, et al., Development of CSNS RFQ. Nuclear Techniques **38(12):120201** (2015). doi: 10.11889/j.0253-3219.2015.hjs.38.120201

[9] H. Liu, J. Peng, K. Gong, et al., The design and construction of CSNS drift tube linac. Nucl. Instrum. Methods Phys. Res. A. **911**, 131-137 (2018). doi: 10.1016/j.nima.2018.10.034

[10] J. Peng, Y. Han, Z. Li, et al., Beam loss studies in the CSNS Linac. In Proc. of HB'23, Geneva, Switzerland, WEA4C1, 297-299 (2023). doi: 10.18429/JACoW-HB2023-WEA4C1

[11] S. Wang, Y. An, S. Fang, et al., An overview of design for CSNS/RCS and beam transport. Sci. China Phys. Mech. Astron. **54(S2)**, 239–244 (2011). doi: 10.1007/s11433-011-4564-x

[12] M. Huang, S. Xu, Y. An, et al., Study on the anti-correlated painting injection scheme for the Rapid Cycling Synchrotron of the China Spallation Neutron Source. Nucl. Instrum. Methods Phys. Res. A. **1007:165408** (2021). doi: 10.1016/j.nima.2021.165408

[13] Q. Li, W. Kang, X. Sun, et al., Key technology of the development of the CSNS/RCS AC dipole magnet. Power Laser and Particle Beams **29(8):085105** (2017). doi: 10.0.46.108/HPLPB201729.160498

[14] X. Qi, J. Zhang, Z. Hao, et al., Magnet Power Supply System for China Spallation Neutron Source. Power Electronics **48(12)**, 8-10 (2014). doi: 10.0.15.129/j.issn.1000-100X.2014.12.002

[15] S. Xu, The Study on the Space Charge Effects of CSNS/RCS. Beijing: University of Chinese Academy of Sciences, 96-99 (2011).

[16] H. Dong, H. Song, Q. Li, el al., The vacuum system of the China spallation neutron source. vacuum **154**, 75-81, (2018). doi: 10.1016/j.vacuum.2018.04.046

[17] R. Williamson, D. Adams, H. Cavanagh, et al., High-Intensity Studies on the ISIS RCS and Their Impact on the Design of ISIS-II. In Proc. of HB'23. Geneva, Switzerland, TUC4I2, 331-337 (2023). doi: 10.18429/JACoW-HB2023-TUC4I2

[18] Accelerator Technical Design Report for High-Intensity Proton Accelerator Facility Project. JAERI Report No. JAERI-Tech 2003-044 and KEK Report No. 2002-13. (2003).

[19] R. Williamson, D. Adams, B. Jones, et al., Simulation of the head-tail instability on the ISIS synchrotron. In Proc. of HB'14. East-Lansing, MI, USA, 113 (2014).

[20] D. W. Posthuma de Boer, B. A. Orton, C. M. Warsop, et al., Development of an Impedance Model for the ISIS Synchrotron and Predictions for the Head-Tail Instability. In Proc. of HB'23. Geneva, Switzerland, TUC4I2, 170-177 (2023). doi: 10.18429/JACoW-HB2023-THA1I2

[21] Y. Shobuda, H. Harada, H. Hotchi, et al., Measurement result of the impedance of the RF-cavity at the RCS in J-PARC. In Proc. of IPAC'15. Richmond, VA, USA, MOPWA058, 255 (2015). doi: 10.18429/JACoW-IPAC2015-MOPWA058

[22] L. Huang, M. Huang, S. Xu, et al., Intense Beam Issues in CSNS Accelerator Beam Commissioning. In Proc. of HB'23. Geneva, Switzerland, MOA1I3, 16-22 (2023). doi: 10.18429/JACoW-HB2023-MOA1I3

[23] S. Xu, H. Liu, J. Peng, et al., Beam commissioning and beam loss control for CSNS accelerators. JINST **15:P07023** (2020). doi: 10.1088/1748-0221/15/07/P07023

[24] L. Huang, Y. An, C. Deng, et al., Upgrade of the sextupole field for beam instability mitigation in rapid cycling synchrotron of China Spallation Neutron Source. Radiat Detect Technol Methods **7**, 550–560 (2023). doi: 10.1007/s41605-023-00428-7

[25] A. W. Chao, Physics of Collective Beam Instabilities in High Energy Accelerators. Wiley, New York, pp. 15 (1993).

[26] H. Xu, C. Lin, N. Wang, et al., Transverse mode-coupling instability with longitudinal impedance. NUCL SCI TECH **35(6):103** (2024). doi: 10.1007/s41365-024-01472-8

[27] J. Su, Y. Liu, S. Tian, et al., Longitudinal impedance measurements and simulations of a three-metal-strip kicker. NUCL SCI TECH **34(4):57** (2023). doi: 10.1007/s41365-023-01212-4

[28] Y. Liu, L. Huang, S. Wang, et al., Impedance and beam instability in RCS/CSNS. High power laser and particle beams **25(2)**, 465-470 (2013). doi: 10.3788/hplpb20132502.0465

[29] L. Huang, Y. Liu, S. Wang, Resistive wall instability in rapid Cycling synchrotron of China spallation neutron source. Nucl. Instrum. Methods in Phys. Res., Sect. A. **728**, 1-5 (2013). doi: 10.1016/j.nima.2013.06.017

[30] L. Huang, S. Wang, Y. Liu, et al., Impedance measurements of the extraction kicker system for the rapid cycling synchrotron of China Spallation Neutron Source. Chinese Physics C **40(4):047002** (2016). doi: 10.1088/1674-1137/40/4/047002

[31] N. Wang, Q. Qin, Resistive-wall impedance of two-layer tube. Phys. Rev. Accel. Beams **10:111003** (2007). doi: 10.1103/PhysRevSTAB.10.111003

[32] Physics design and technology development of CSNS accelerator. Institute of High Energy Physics, IHEP Report, Beijing, China (2010).

[33] L. Huang, S. Wang, S. Xu, et al., Source of instability in the rapid cycling synchrotron of the China spallation neutron source. Eur. Phys. J. Plus **140(1):71** (2025). doi: 10.1140/epjp/s13360-025-05997-8

[34] B. Zotter, Longitudinal instabilities of charged particle beams inside cylindrical walls of finite thickness. Particle Accelerators **1**, 311-326 (1970).

[35] A. W. Chao and M. Tigner, Handbook of Accelerators physics. World scientific, Singapore, 205 (1999).

[36] Y. H. Chin, S. Lee, K. Takata, et al., Impedance generated by a ceramic chamber with RF shields and TiN coating. In proc. of HB'06, Tsukuba, Japan, TUBX01 (2006).

[37] N. Wang, Coupling impedance and collective e ects in the RCS ring of the China spallation neutron source. Ph. D thesis, University of Chinese Academy of Sciences, (2009).

[38] F. Roncarolo, F. Caspers, T. Kroyer, et al., Comparison between laboratory measurements, simulations and analytical predictions of the transverse wall impedance at low frequencies. Phys. Rev. Accel. Beams **12:084401** (2009).doi: 10.1103/PhysRevSTAB.12.084401

[39] V. Danilov, S. Henderson, A. Burov, et al., An improved impedance model of metallic coatings. In proc. of the EPAC'02, 1464-1466 (2002).

[40] CST STUDIO SUITE website. https://www.3ds.com/products/simulia/cst-studio-suite

[41] K. Y. Ng, Physics of Intensity Dependent Beam Instabilities. World Scientific, Singapore, (2006).

[42] F. Caspers. Bench methods for beam-coupling impedance measurement. CERN report, CERN PS/88-59 (1988).

[43] A. Mostacci, F. Caspers; U. Iriso, et al., Bench measurements of low frequency transverse impedance. In proc. of PAC'03, pp. 1801-1803 (2003).

[44] H. Hotchi, H. Harada, N. Hayashi, et al., Achievement of a low-loss 1-MW beam operation in the 3-GeV rapid cycling synchrotron of the Japan Proton Accelerator Research Complex. Phys. Rev. Accel. Beams **20:060402** (2017). doi: 10.1103/PhysRevAccelBeams.20.060402